5

Flow Visualization and Proper Orthogonal Decomposition of Aeroelastic Phenomena

Thomas Andrianne, Norizham Abdul Razak and Grigorios Dimitriadis
Aerospace and Mechanical Engineering Department, Faculty of Applied Sciences, University of Liège
Belgium

1. Introduction

The modal decomposition of unsteady flowfields was proposed in the 1990s by several authors, e.g. Hall (1994) or Dowell et al. (1998). Proper Orthogonal Decomposition (POD) is one method that can be used in order to perform this modal decomposition; it became popular for aerodynamics research in the 2000s, starting with Tang et al. (2001), although it was first proposed for use in fluid dynamics in the 1960s by Lumley (1967).
The basic principle of POD is the creation of a mathematical model of an unsteady flow that decouples the spatial from the temporal variations. A 2D flowfield described by the horizontal velocity $u(x,y,t)$ and the vertical flow velocity $v(x,y,t)$ can thus be expressed as

$$\begin{aligned} u(x,y,t) &= \bar{u}(x,y) + u'(x,y,t) = \bar{u}(x,y) + \sum_{i=1}^{M} q_i(t)\phi_{u,i}(x,y) \\ v(x,y,t) &= \bar{v}(x,y) + v'(x,y,t) = \bar{v}(x,y) + \sum_{i=1}^{M} q_i(t)\phi_{v,i}(x,y) \end{aligned} \tag{1}$$

where $\bar{u}(x,y)$ and $\bar{v}(x,y)$ are obtained by time averaging the flowfield over M time instances, while $u'(x,y,t)$ and $v'(x,y,t)$ are time-dependent fluctuations from the mean. These fluctuations are decomposed using M mode shapes $\phi_{u,i}(x,y)$, $\phi_{v,i}(x,y)$ and M generalized coordinates $q_i(t)$. For a reduced order model, the number of modes, $N << M$, is to be chosen as a compromise between model simplicity and model accuracy. The principle of the POD technique is to extract the most energetic modes that capture most of the unsteady flow energy. The POD technique has been used to decompose several types of aerodynamic flows, such as the flow behind a disk (Tutkun et al., 2008), the flow past a delta wing (Cipolla et al., 1998), the unsteady flow impinging on an aircraft tail behind a delta wing (Kim et al., 2005), the unsteady flow around a F-16 fighter configuration (Lie & Farhat, 2007) and others.
It should be noted that there are two types of POD research being carried out at the moment. The first concerns the decomposition of flowfields observed in experiments in order to better understand the flow mechanisms and physics underlying these flows. The second type of research concerns the Reduced Order Modelling of unsteady Computational Fluid Dynamic (CFD) simulations or even, CFD/CSD (Computational Structural Dynamics) simulations,

in order to produce simplified but representative models that can be used in practical applications such as aircraft design.
The work of interest here is the of first type, i.e. the experimental work. It is usually combined with high-speed Particle Image Velocimetry (PIV) measurements, although there are examples of other instrumentation being used, such as hot wire rakes (Tutkun et al., 2008). The limitation of all research works published on the subject is that the models around which the flowfield is measured are always static or rotating at constant velocity. Additionally, only one source of flow unsteadiness is ever considered.
The objective of the present work is to expand the methodology of the application of POD to experimental flowfields. There are two aspects to this expansion:

1. Allow the models to oscillate. The source of the unsteadiness will then be the movement of the model, as well as any unsteadiness due to flow separation.
2. Study the interaction between the different sources of unsteadiness. In particular observe how the modes generated by one source of unsteadiness interact with the modes generated by the other. Determine if it is possible to separate the structural from the aerodynamic sources of unsteadiness.

2. Basics of Proper Orthogonal flow decomposition

Observation of an unsteady flow by PIV will, in general, yield M shapshots of a 2D section of the flowfield at times $t_1, \ldots, t_M$. These snapshots will usually feature information on the $u(x, y, t)$ and $v(x, y, t)$ velocity vectors although other information can also be obtained (e.g. vorticity). The velocity vectors will be available on a spatial grid of size $n_y \times n_x$, i.e. there will be n_y gridpoints in the y direction with spacing δy and n_x in the x direction with spacing δx. Therefore, $u(x, y, t)$ and $v(x, y, t)$, will be available in discrete form, i.e. in the form of $n_y \times n_x \times M$ real arrays.
The time-averaged flow is represented by $(\bar{u}(x, y), \bar{v}(x, y))$, where

$$\bar{u}(x, y) = \frac{1}{M} \sum_{i=1}^{M} u(x, y, t_i)$$
$$\bar{v}(x, y) = \frac{1}{M} \sum_{i=1}^{M} v(x, y, t_i)$$

and the unsteady velocity components are obtained simply from

$$u'(x, y, t) = u(x, y, t) - \bar{u}(x, y)$$
$$v'(x, y, t) = v(x, y, t) - \bar{v}(x, y) \tag{2}$$

The Proper Orthogonal Decomposition procedure is then applied on the data matrix $\mathbf{C}$, the auto-correlation matrix of the total energy in the flow at every instance in time. For a continuous flow,

$$C(t_1, t_2) = \frac{1}{M} \int \int \left(u'(x, y, t_1) u'(x, y, t_2) + v'(x, y, t_1) v'(x, y, t_2) \right) dxdy \tag{3}$$

For a discrete flow, the integrals become summations. Using trapezoidal integration,

$$C_{i,j} = \frac{1}{M} \sum_{k=1}^{n_y-1} (G_{i,j,k} + G_{i,j,k+1})\delta y/2 \tag{4}$$

where $C_{i,j}$ is the element in the ith line and jth column of $\mathbf{C}$, $G_{i,j,k} = \sum_{l=1}^{n_x-1}(F_{i,j,k,l} + F_{i,j,k,l+1})\delta x/2$, $F_{i,j,k,l} = \left(u'_{k,l,i}u'_{k,l,j} + v'_{k,l,i}v'_{k,l,j}\right)$ and the notation $u'_{k,l,i}$ is shorthand for $u'(x_k, y_l, t_i)$. Higher order integration schemes can also be used.
The Proper Orthogonal Decomposition process requires the solution of the eigenvalue problem

$$\mathbf{CA} = \lambda\mathbf{A} \tag{5}$$

where $\mathbf{A}$ are the matrix of eigenvectors of the $\mathbf{C}$ matrix and λ are its eigenvalues. If the eigenvectors are normalized in the form $\mathbf{a}_i/\sqrt{\lambda_i M}$, where $\mathbf{a}_i$ is the ith column of $\mathbf{A}$, then they will form an orthonormal basis. The mode shapes $\phi_{u,i}$ and $\phi_{v,i}$ can be constructed from

$$\begin{aligned}\phi_{u,i}(x,y) &= \frac{1}{\sqrt{\lambda_i M}} \sum_{m=1}^{M} u'(x,y,t_m)a_{m,i} \\ \phi_{v,i}(x,y) &= \frac{1}{\sqrt{\lambda_i M}} \sum_{m=1}^{M} v'(x,y,t_m)a_{m,i}\end{aligned} \tag{6}$$

where $a_{m,i}$ is the mth element of the ith eigenvector of $\mathbf{C}$. The mode shapes are only functions of space but can be used to describe the unsteady flowfield when combined with the generalized coordinates $q_i(t)$, which can be obtained from

$$q_i(t) = \int\int \left(u'(x,y,t)\phi_{u,i}(x,y) + v'(x,y,t)\phi_{v,i}(x,y)\right) dxdy \tag{7}$$

or from the discrete version of this equation.
There are M eigenvalues and hence M sets of mode shapes and generalized coordinates. However, the aim of POD is to create a reduced order model, using only the first N modes that contain most of the fluctuating flow energy. To this end, the quantity $\lambda_i/\sum_{i=1}^{M}\lambda_i$ can be inspected, assuming that λ_i is ordered from highest to lowest eigenvalue. Kim et al. (2005) note that it should be $\sum_{i=1}^{M}\lambda_i = 1$, however this depends on the scaling used by the eigenvalue estimator, so looking at the ratio $\lambda_i/\sum_{i=1}^{M}\lambda_i$ is safer. If the first N eigenvalues are chosen, that have ratios higher than, say, 10% then a N mode model will be created.
Finally, the N-mode approximation of the complete velocity field can be reconstructed from the N retained modes using equation 1

$$\begin{aligned}u^*(x,y,t) &= \bar{u}(x,y) + \sum_{i=1}^{N} q_i(t)\phi_{u,i}(x,y) \\ v^*(x,y,t) &= \bar{v}(x,y) + \sum_{i=1}^{N} q_i(t)\phi_{v,i}(x,y)\end{aligned}$$

The POD procedure described above will be applied (with some modifications) to experimentally observed unsteady flows behind a circular cylinder at conditions both near to and far from resonance.

3. Experimental setup

The experiments were carried out in the multi-disciplinary low speed wind tunnel of the University of Liège. The Aeronautical test section of the wind tunnel was used, which measures 2m $\times$ 1.5m $\times$ 5m (width $\times$ height $\times$ length) and has a maximum airspeed of 60m/s.

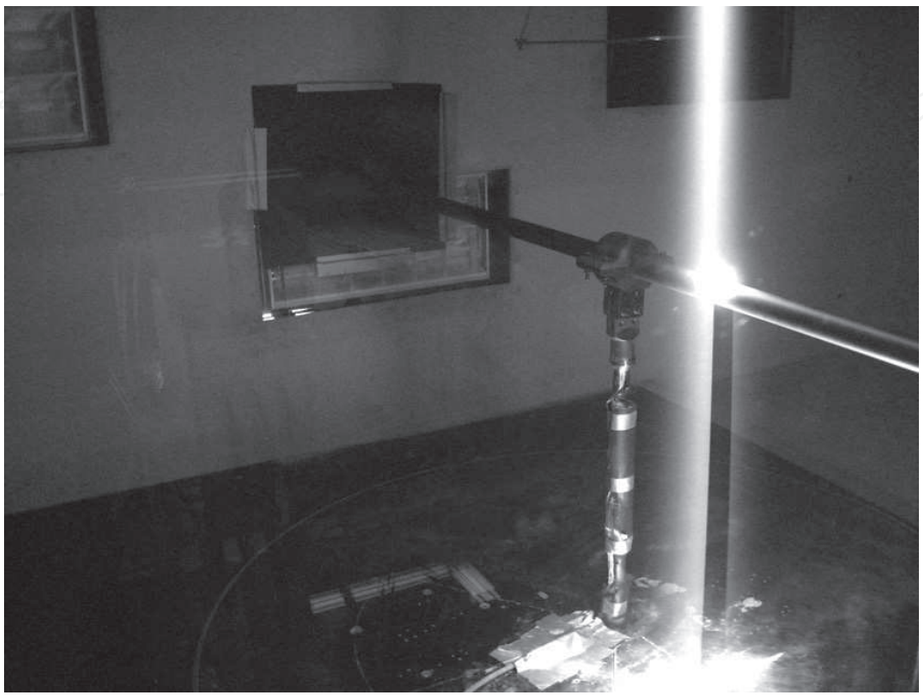

Fig. 1. Laser sheet illuminating 2D section of flow around a cylinder

A circular cylinder of 36mm diameter and 1.32m span was placed in the wind tunnel, supported by its mid-span point near the middle of the test section. The cylinder was made of aluminium tube and painted matt black. The cylinder is rigidly supported but is flexible itself. Its first symmetric bending mode has a frequency of around 70Hz. Therefore, it is expected that when the frequency of the Von Karman vortex street behind the cylinder matches the first bending frequency, the free ends of the cylinder will oscillate quite visibly. Away from resonance, the cylinder will be static. This setup is ideal for the purposes of the present investigation, as it allows the examination of the unsteady flow behind both a static and a vibrating object.

4. PIV system setup

The PIV system used for these experiments consists of the following components:

1. A Litron LDY301-PIV Q-switched laser system. It is a dual power, dual cavity laser with a wavelength of 527nm, switching at 1000Hz. The two laser beams contain 2 $\times$ 10mJ of energy.
2. Optical modules for producing a laser sheet.
3. A Phantom V9.1 camera with a maximum resolution of 1600 $\times$ 1200 pixels at a frequency of 1KHz and 6GB of internal memory buffer.

4. A timer box for synchronizing the laser with the camera.
5. A seeding generator with 3 bar back pressure suitable for PIV particle generation.
6. Dantec Dynamics Studio PIV data acquisition and analysis software.
7. A high specification Personal Computer.

In practice, the system is capable of capturing PIV data in a window of around 13×11cm at a frequency of 1000Hz.
The laser sheet was placed on the side of the cylinder nearest to the working section's observation window and aligned with the airflow, so as to illuminate a 2D section of flow around the cylinder. The laser sheet position can be seen in figure 1. Notice that the centre of the laser sheet lies aft of the cylinder. The very sharp shadow under the cylinder is also worth noting.

4.1 PIV results

Figure 2 shows a snapshot of the illuminated particles around the cylinder. It can be seen that the laser illuminates the aft upper section of the cylinder itself (white arc) as well as seeded particles on the upper surface of the cylinder and in the wake. Evidently, there are no illuminated particles in the shaded area under the cylinder.

Fig. 2. Illuminated particles around the cylinder

The PIV system takes two such snapshots at a very short time interval, typically $1 - 1000\mu$s. A region of interest (ROI) is defined in the snapshots. This ROI is further divided into subregions (e.g. 64 x 64 pixels). The motion of the particles inside each subregion of the first snapshot is correlated to the second snapshot. The aim of the analysis is to decide where each subregion of photo 1 has moved to on photo 2. Thus, a velocity vector is placed in the centre of each subregion, representing the global motion of the particles inside the latter. The entire process is carried out by means of the Dynamics Studio PIV software and requires calibration data consisting of the free stream airspeed or a characteristic length, in this case the cylinder diameter.
The end result of the PIV data reduction process is a velocity vector field calculated at each instance in time for which the visualization took place, as shown in figure 3. The image correlation process can sometimes lead to the calculation of bad vectors (outliers); these are detected and replaced by averages of all the neighboring vectors.
PIV visualizations for the circular cylinder were carried out at airspeeds from 10 to 20m/s, at a sampling frequency of 1000Hz and sampling times from 0.1s to 4s. The recovered unsteady

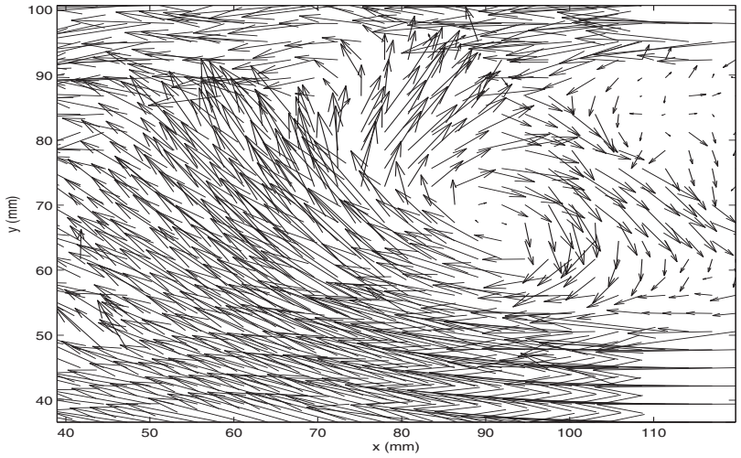

Fig. 3. Computed velocity vectors for a sample snapshot

vector fields had a resolution of 24 gridpoints in the y-direction and 41 in the x-direction. Therefore, the sizes of the u and v matrices ranged from $24 \times 41 \times 100$ to $24 \times 41 \times 4000$.

4.1.1 Flow frequency variation with airspeed

In order to verify that the PIV system and POD decomposition analysis are performing correctly, a large number of PIV measurements were carried out at airspeeds between 4m/s and 26m/s. The flow frequencies recovered by the POD method for all these measurements were then compared to the theoretical frequencies, assuming that the cylinder has a Strouhal number of 0.2. This comparison can be seen in figure 4, where the experimentally estimated frequencies are plotted as stars with error bars and the theoretical frequency is plotted as a dashed sloped line. The error bars represent the frequency increment, equal to the sampling frequency divided by the number of time measurements M and is equal to 2.02Hz.

Figure 4 shows that the frequencies estimated from the decomposed PIV measurements are in good agreement with the theoretical predictions. It can be concluded that both the instrumentation and the POD analysis were correctly operated. The two dotted lines in the figure represent the airspeed limits at which significant cylinder vibration amplitudes were observed. Indeed, resonance phenomena were observed at airspeeds between 13.5m/s and 18m/s, corresponding to vortex shedding frequencies of 70-105Hz. The lock-in phenomenon, whereby the flow frequency adapts itself to the structure's natural frequency throughout the resonance airspeed range, is not evident in this data. The reason for this absence of lock-in is that the measurements used for constructing figure 4 were taken close to the cylinder's midpoint, as seen in figure 1. At this location the amplitudes of the vertical vibration are small and have no impact on the shedding process. The frequency of the latter follows the linear Strouhal relation.

4.2 POD analysis

At the end of the PIV data treatment, a set of $u(x, y, t)$ and $v(x, y, t)$ matrices were obtained for each tested airspeed. These matrices where then analyzed using the POD procedure described in section 2. Sample results from three airspeeds are presented and discussed in this section. These are labeled as:

- Test 1: Free stream airspeed of 18.8m/s, sampling frequency of 1000Hz, sampling time of 0.298s, PIV laser sheet at 0.2m from the cylinder's midpoint.

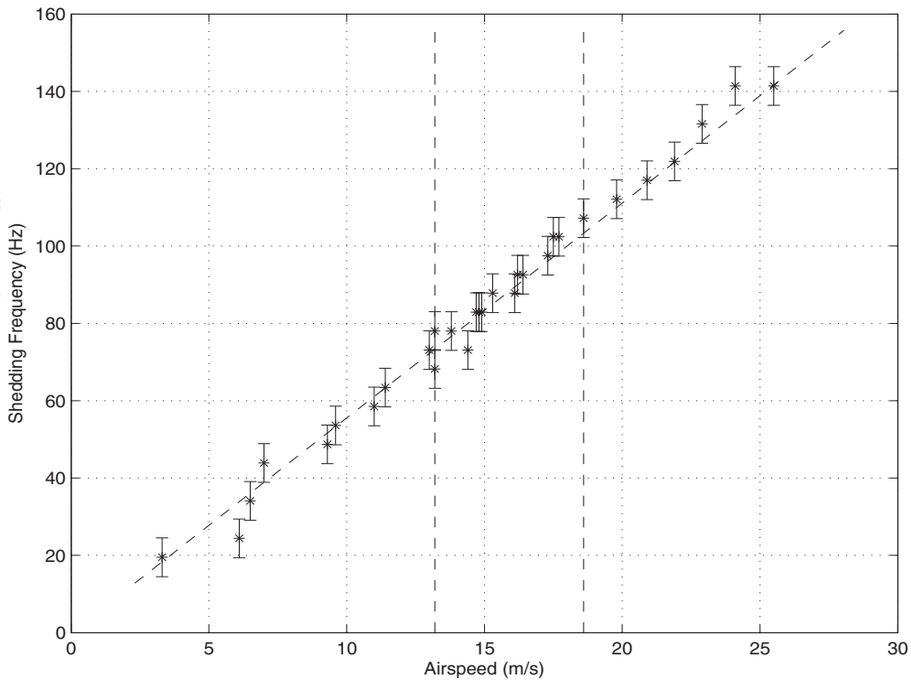

Fig. 4. Comparison of estimated frequencies to theoretical frequencies

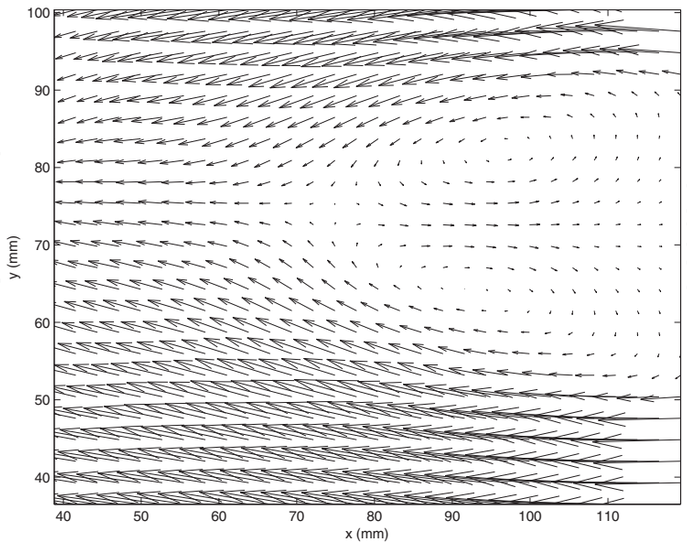

Fig. 5. Mean flow vectors for test 1

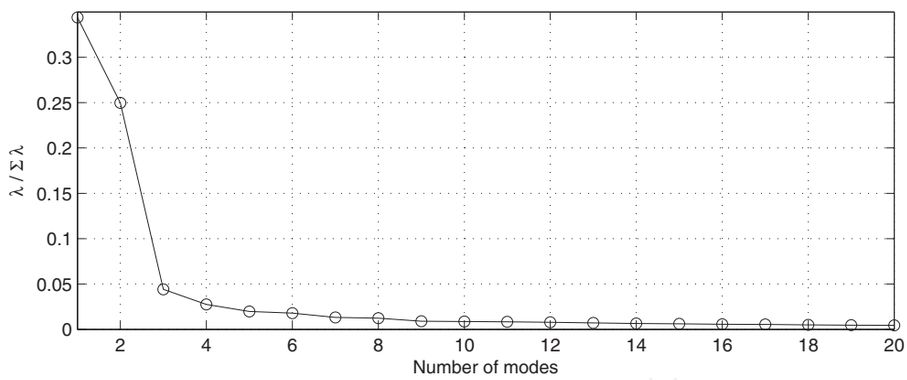

Fig. 6. Eigenvalue ratios for the first 20 eigenvalues for test 1

- Test 2: Free stream airspeed of 13m/s, sampling frequency of 1000Hz, sampling time of 0.099s, PIV laser sheet at 0.2m from the cylinder's midpoint.
- Test 3: Free stream airspeed of 13.9m/s, sampling frequency of 1000Hz, sampling time of 0.099s, PIV laser sheet at 0.2m from the cylinder's midpoint.
- Test 4: Free stream airspeed of 14.8m/s, sampling frequency of 1000Hz, sampling time of 0.099s, PIV laser sheet at 0.4m from the cylinder's midpoint

The Reynolds numbers for the three tests range from 40,000 to 55,000, which puts the flowfield in the 'transitional in the shear layer' category. In other words, the boundary layer on the cylinder's surface is expected to be laminar. After separation, there is periodic ejection of vortices in the wake, as in the case of laminar vortex shedding, but the shear layer causing this ejection is transitional, giving rise to small turbulent eddies.
Test 1 is used as the reference test, as it lies very far from aero-structural resonance and, therefore, there is negligible cylinder movement. Test 4 lies right on resonance and the cylinder vibrates significantly at the PIV measurement position. For all the tests, the first step in the POD procedure was to define the region of interest, so as not to include in the POD calculations the velocity vectors under the cylinder, which are not observable. The region of interest was therefore limited to a point just downstream of the cylinder.

4.2.1 Test 1

The next step in the POD procedure for Test 1 was to calculated the mean flow. This calculation involved the time averaging of the $u(x,y,t)$ and $v(x,y,t)$ matrices, leading to the mean flow shown in figure 5. It can be seen that the mean flow is essentially an area of slow, recirculating flow, located just behind the cylinder. In other words, it can be seen as the steady wake, to which an unsteady wake is superimposed.
Once the mean flow was subtracted from $u(x,y,t)$ and $v(x,y,t)$ the unsteady vector fields $u'(x,y,t)$ and $v'(x,y,t)$ were obtained and Proper Orthogonal Decomposition was applied. The eigenvalue ratios $\lambda_i / \sum_{i=1}^{M} \lambda_i$ obtained for the first 20 modes are shown in figure 6. It can be seen that only the first two eigenvalues have significant contributions to the total energy in the unsteady flow, of 35% and 25% respectively. All higher eigenvalues have contributions of less than 5% and can therefore be neglected.
The mode shapes associated to the two retained eigenvalues are shown in figure 7, plotted as filled contour plots. Subfigure 7(a) plots the values of $\phi_u(x,y)$ (left) and $\phi_v(x,y)$ (right) for mode 1 as a filled contour plot, black signifying a low value and white signifying a high

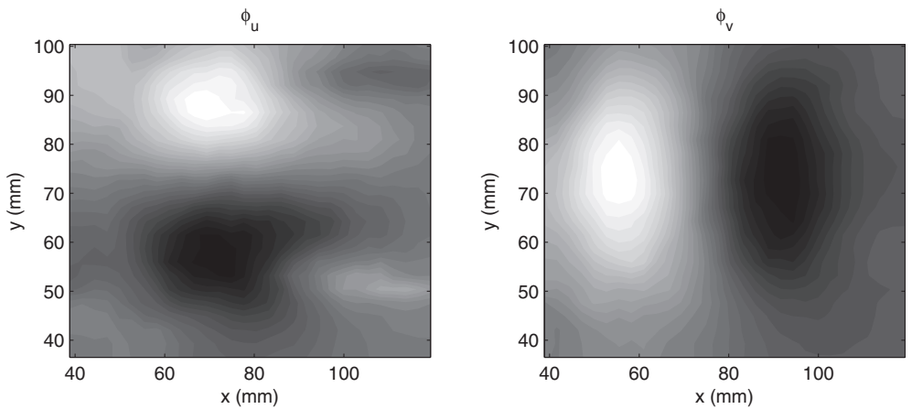

(a) Mode 1

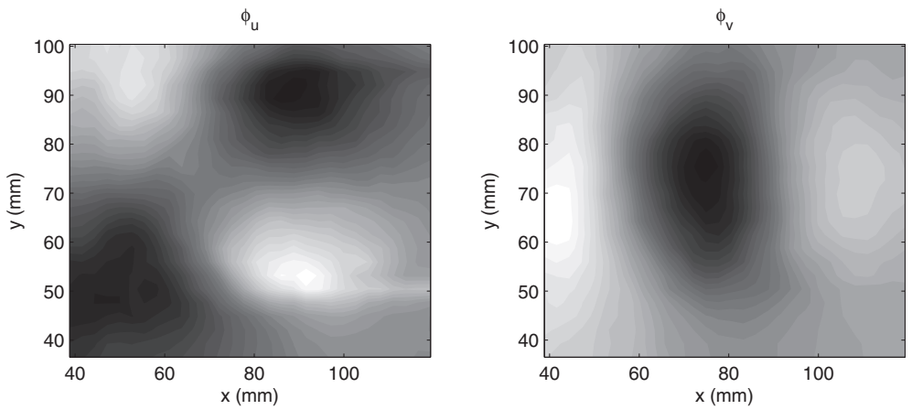

(b) Mode 2

Fig. 7. The first two mode shapes for test 1

value. Subfigure 7(b) depicts the same information for mode 2. The horizontal distance between a maximum and a minimum grows from 30mm to 40mm with distance downstream. The vertical distance increases with downstream distance from 30mm to 46mm. If the mode shapes are assumed to be periodic, i.e. repeatable further downstream, then the two modes are separated by 1/4 of a period. It should be noted that the distances between maxima and minima are not constant because the measurement is just behind the cylinder, where there are large variations in the mean flow, as seen in figure 5. It is likely that the distances between maxima and minima are stabilized further downstream.

Figure 8 shows the variation in time of the two retained generalized coordinates. It can be seen that the two generalized coordinates have the same fundamental frequency of 107.5Hz. Furthermore, they are both subjected to a beating phenomenon, with the response amplitudes dropping momentarily at around 0.12s and again at around 0.3s. This beating demonstrates that the flow is quasi-periodic, with significant variations in amplitude occurring momentarily. This quasi-periodic nature is justified by the fact that the flow is transitional in the shear layer and there are small turbulent eddies absorbing some of the flow energy.

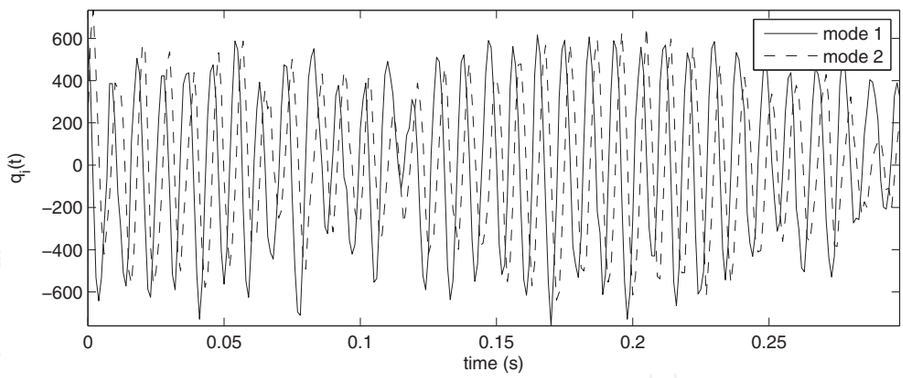

Fig. 8. Variation in time of the two retained generalized coordinates, Test 1

In fact, the two mode shapes of figure 7 are the dominant modes and can be viewed as 'laminar' modes. The modes that have been neglected can be viewed as 'turbulent' modes, which contain little energy over the complete time history but can momentarily absorb energy from the dominant modes. This is exactly what happens in the case of this test. At time indices of 0.12s and 0.3s, the response amplitude of modes 1 and 2 drops significantly; simultaneously the response amplitude of mode 3 increases visibly, as shown in figure 9(a), which plots the variation of generalized coordinate $q_3(t)$ with time. It can be clearly seen that the maxima of this mode occur at 0.12s and 0.3s.
The mode shape for mode 3 can be seen in figure 9(b). It is clear that this mode shape is significantly noisier than the mode shapes of the first two modes, shown in figure 7. This noisiness is consistent with the hypothesis that mode 3 represents turbulent flow energy. It should be mentioned that higher modes do not demonstrate any clear increases in amplitude at 0.12s and 0.3s. Therefore, a complete model of the flow of Test 1 will contain:

- two modes if only the laminar flow is of interest
- three modes if it is desired to account for some of the energy momentarily lost by the laminar modes

4.2.2 Test 2

Test 2 is similar to Test 1 in the sense that resonance is not occurring yet; however, the condition is much closer to resonance than Test 1 and the amplitude of vibration of the cylinder is small but noticeable. Under these circumstances, the effect of evaluating a mean flow and subtracting it from the total vector field must be revised. In effect, as the mean flow is the steady wake behind the cylinder, if the cylinder oscillates by a significant amount, then the concept of a steady wake is no longer valid and the mean flow should not be evaluated. In other words, while it is still possible to calculate values for $\bar{u}$ and $\bar{v}$ over the entire time history, these values will not be the same over a different time history. In essence, the movement of the cylinder is an excitation force that is applied to the fluid; it will respond at the excitation frequency and at higher harmonics but there will be no response component with zero frequency.
Nevertheless, if the amplitude of oscillation is very small, then evaluating and subtracting the mean flow will not cause big errors in the POD procedure. For Test 2, the POD method was applied twice, the first time after subtracting the mean flow and the second after subtracting only the wind tunnel free stream, U. In other words, in the first application the POD analysis

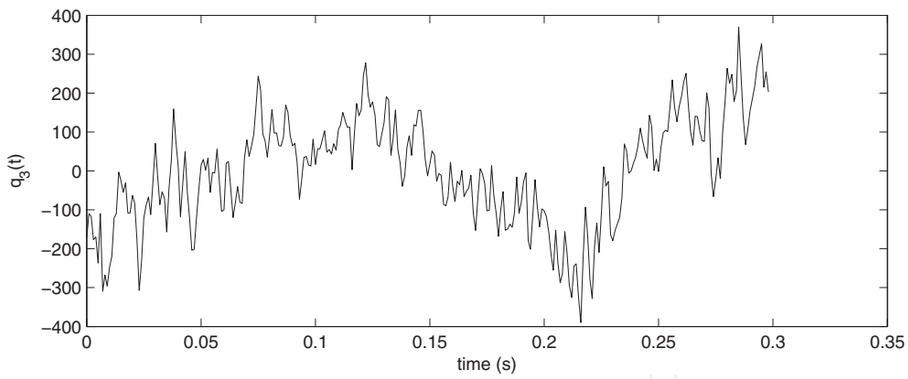

(a) $q_3(t)$

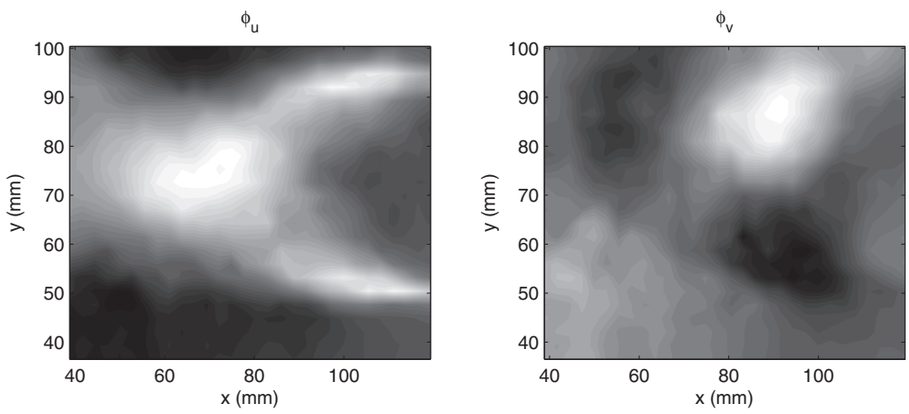

(b) Mode 3

Fig. 9. The third mode for test 1

was carried out on u' and v' using equations 3 to 7 while in the second it was carried out on $u - U$ and v, such that

$$C(t_1, t_2) = \frac{1}{M} \int \int \left((u(x, y, t_1) - U)(u(x, y, t_2) - U) + v(x, y, t_1) v(x, y, t_2) \right) dxdy \tag{8}$$

with

$$\phi_{u,i}(x, y) = \frac{1}{\sqrt{\lambda_i M}} \sum_{m=1}^{M} (u(x, y, t_m) - U) a_{m,i}$$

$$\phi_{v,i}(x, y) = \frac{1}{\sqrt{\lambda_i M}} \sum_{m=1}^{M} v(x, y, t_m) a_{m,i} \tag{9}$$

and

$$q_i(t) = \int \int \left((u(x, y, t) - U) \phi_{u,i}(x, y) + v(x, y, t) \phi_{v,i}(x, y) \right) dxdy \tag{10}$$

For the first application, the number of retained modes was 2, i.e. only the laminar unsteady flow modes were found to be significant; the resulting mode shapes were qualitatively similar to those obtained for Test 1 (figure 7). For the second application, the number of

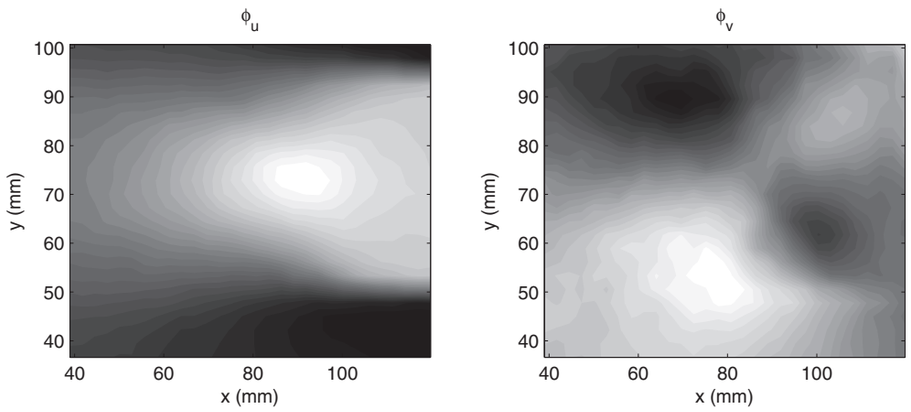

(a) Mode 1

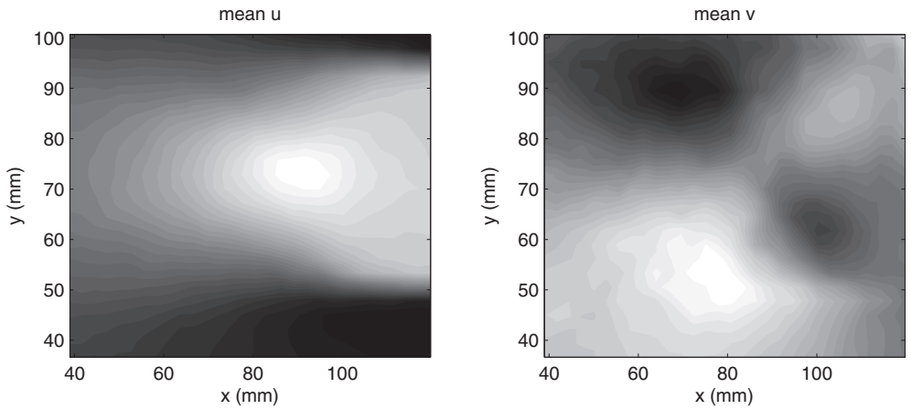

(b) Mean flow

Fig. 10. The first mode shape for test 2 (top) compared to the mean flow (bottom)

retained modes was 3. The first mode represented the mean flow while the other two modes represented the laminar unsteady flow and were very similar to the modes of the first application and, consequently, of figure 7. It is interesting to compare the mean flow subtracted from the data in the first application to the first mode obtained from the second application. Figure 10 shows contour plots of the first mode $\phi_{u,1}$ and $\phi_{u,2}$ evaluated from the application of POD to $u - U$ and v (top two plots) and of the mean flow components $\bar{u}$ and $\bar{v}$ (bottom plots). It can be seen that the two sets of contour plots are very similar. Therefore, the POD procedure described by equations 8 to 10 will calculate the mean flow as the most energetic mode.

This is quite an interesting result because it suggests that there is no need to subtract the mean flow. If there is a steady component to the flow, then it will be identified automatically as the first mode. If there is no steady component, then equations 8 to 10 should be used anyway. Figure 11 shows the time response of the three resulting generalized coordinates. It can be seen that the generalized coordinate of the first mode is nearly constant with a value of around 600, while the coordinates of the other two modes oscillate around zero. It is clear that the POD procedure can differentiate between steady and unsteady responses.

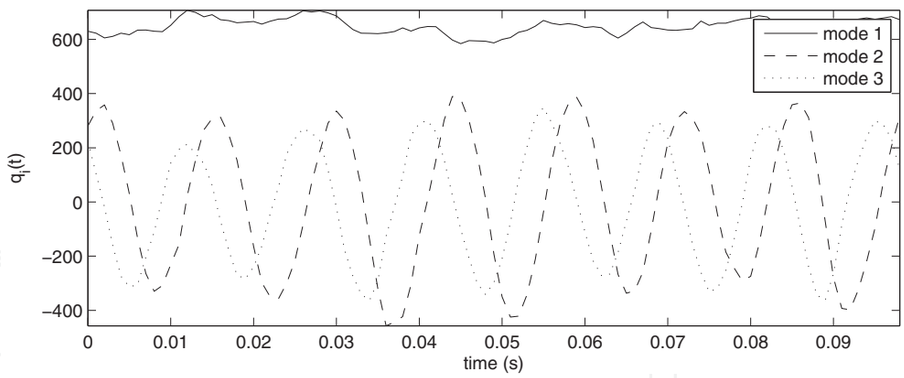

Fig. 11. Variation in time of the three retained generalized coordinates, Test 2

4.2.3 Test 3

For Test 3 the POD procedure was carried out only using equations 8 to 10. As mentioned before, Test 3 gave rise to significant amplitudes of cylinder vibration as the flow frequency was very close to a natural frequency of the cylinder. Again, three modes were retained, one representing a mean flow and two representing the laminar oscillating flow.

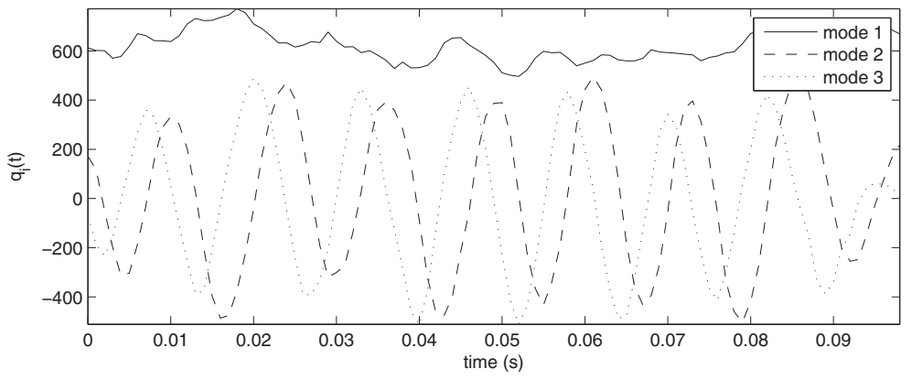

Fig. 12. Variation in time of the three retained generalized coordinates, Test 3

The response amplitudes of the three generalized coordinates were significantly higher than in the case of Test 2, as seen in figure 12. Even the generalized coordinate of mode 1 is far more unsteady, although its variation in time is not periodic. This aperiodic variation suggests that there is a component of the cylinder vibration in the flow data but it is of the same order as the turbulent disturbances and/or experimental error. This was indeed the case, as the measurement point was close to the cylinder's midpoint (see figure 1), therefore the local vibration amplitude was small, of the order of less than 1mm.

4.2.4 Test 4

The final test was carried out at a slightly higher airspeed but, crucially, the PIV laser sheet was positioned at a span-wise point further from the cylinder's midpoint than for the other three tests. At this particular span-wise position, the cylinder was vibrating significantly, with an amplitude of nearly 2mm and a frequency of 70.5Hz.

The POD procedure was again applied using equations 8 to 10, i.e. without subtracting the mean flow. The resulting mode shapes were similar to those obtained during Test 3. The

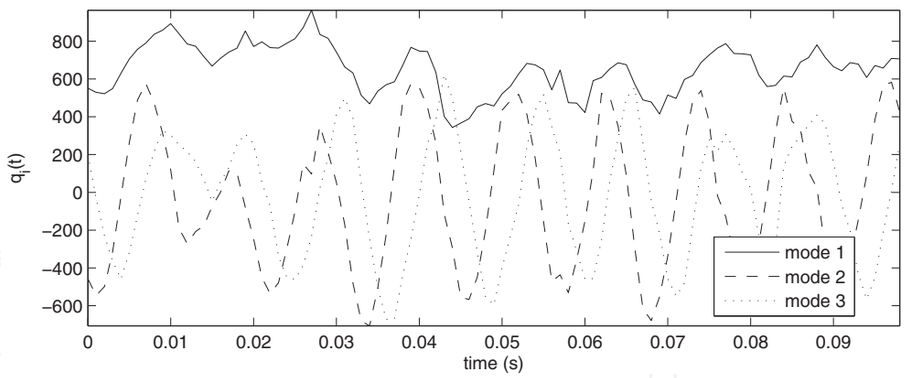

Fig. 13. Variation in time of the three retained generalized coordinates, Test 4

resulting generalized coordinates are plotted on figure 13. It can be clearly seen that the response of the first generalized coordinate is now much more oscillatory than in the case of figure 12. Furthermore, despite the randomness of this response, there is a clear periodic component at a frequency close to that of the oscillating modes.

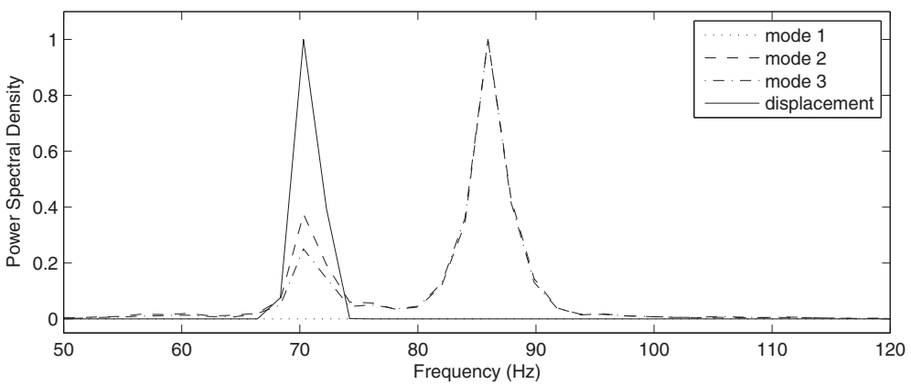

Fig. 14. Power Spectral Density plots of the generalized coordinates and the cylinder displacement.

The observations of Test 4 suggest that POD can decompose flowfields that feature unsteadiness due to the presence of both separated flow and structural motion of the wind tunnel model. However, for this decomposition to be successful, the response amplitude of the structure must be significantly higher than the size of the turbulent eddies. In such cases, straightforward POD will result in generalized coordinates that contain the response frequencies of both the separated flow and the structural motion. Figure 14 shows Power Spectral Densities (PSD) of the $q_i(t)$ and $z(t)$ signals, $z(t)$ being the vertical displacement time history of the cylinder at the PIV measurement position. The PSDs were calculated using the Welch method, with a Hamming window 512 samples long and 50% overlap. The cylinder's displacement response clearly contains only one frequency component at 70.5Hz. The generalized coordinates feature two frequency components, one at 70.5Hz and a stronger one at 85.9Hz. It can be inferred that 70.5Hz is the structural response frequency while 85.9Hz is the vortex shedding frequency. The Strouhal frequency at the Test 4 airspeed is 82.2Hz if a Strouhal number of 0.2 is assumed (see figure 4), i.e. quite close to 85.9Hz.

The generalized coordinates can be seen as the responses in time of the fluid due to both flow unsteadiness and cylinder motion. Furthermore, the cylinder motion can be seen as an external excitation acting on the fluid. Therefore, it possible to set up an input-output POD model, whereby the input is the cylinder motion and the outputs are the generalized coordinates. Frequency Response Functions (FRF) can then be created of the form

$$H_i(\omega) = \frac{Q_i(\omega)}{Z(\omega)} \tag{11}$$

where H_i is the ith FRF, Q_i is the ith generalized coordinate in the frequency domain, Z is the cylinder displacement in the frequency domain and ω is the radial frequency. Such FRFs can be estimated using a Welch-type windowed approach and involving cross and auto-correlations of the outputs and input.

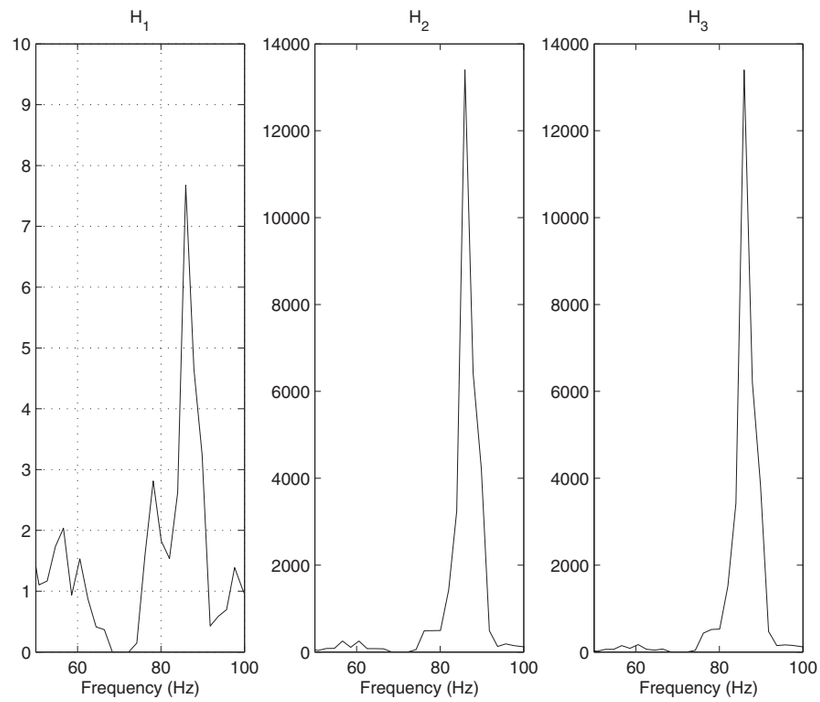

Fig. 15. FRFs between the generalized coordinates and the cylinder displacement.

Figure 15 shows the FRFs estimated for the first three modes of Test 4. It can be seen that the main frequency component of all FRFs is the vortex shedding frequency at 85.9Hz, in the frequency range between 50 and 100Hz. The FRF of mode 1, H_1, features several other peaks but these are most likely noise; for this mode the main frequency component lies at 0Hz, since the mode mainly reflects the mean flow.

4.2.5 Mode shapes variation with airspeed

Here, the variation of the modes shapes with airspeed will be discussed. Only the free stream is subtracted from the local velocity field for the results in this subsection, not the mean flow. It was observed that the first three modes, i.e. the steady flow and the two laminar modes, change very little in shape with airspeed.

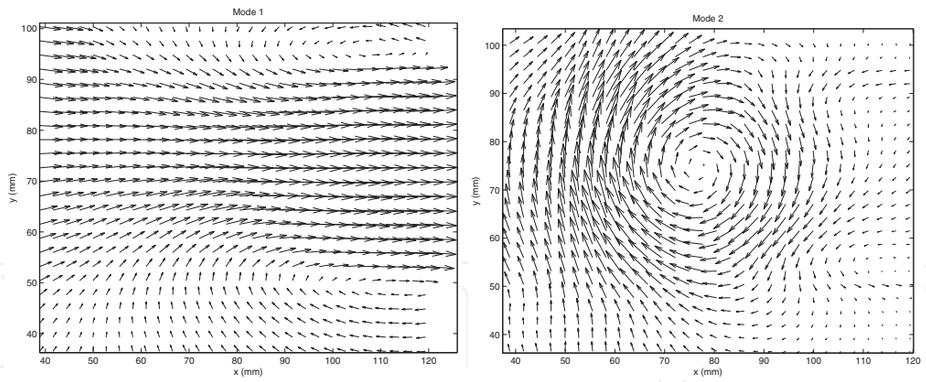

(a) Mode 1 (b) Mode 2

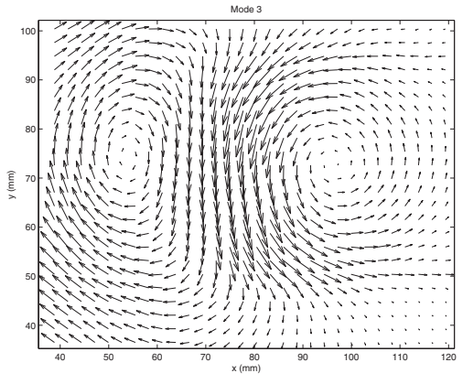

(c) Mode 3

Fig. 16. Vector plots of the first three mode shapes

Figure 16 shows plots of the first three modes in vector form, whereby the vectors' horizontal component is taken as $\phi_{u,i}(x,y)$ and the vertical one as $\phi_{v,i}(x,y)$. Mode one (figure 16(a)) consists of two areas of recirculation behind the top and the bottom of the cylinder. Between them, they cause a significant area of flow towards the cylinder with a height approximately equal to the cylinder's diameter. Mode two (figure 16(b)) consists of a large vortex, positioned approximately one diameter behind the cylinder and centered on the cylinder's centerline. It is accompanied by two much smaller areas of recirculation lying just behind the top and bottom of the cylinder. Mode 3 (figure 16(c)) consists of two counter-rotating vortices at approximately half a diameter (the strongest) and one diameter (the weakest) behind the cylinder. They are both lying on the cylinder's centerline. As mentioned above, these three modes remain largely unaffected by the airspeed.

Figure 17 shows vector plots of mode 4 obtained for the four different tests, i.e. at four different airspeeds. It can be seen that all mode shapes are different. The mode shape for Test 1consists of four vortices; for Test 2 of three vortices, one of which is very weak; for Test 3 the mode shape consists of three vortices again but in a different arrangement; finally, for Test 4 the number of vortices is difficult to determine because they are quite weak and small.

The reason for the change in mode shape 4 with test airspeed may be numerical rather than physical. In fact, mode shapes very similar to that of figure 17(a) appeared as mode 6 in Test 3 and mode 5 in Test 4. Therefore, the same mode shape can be preserved but its

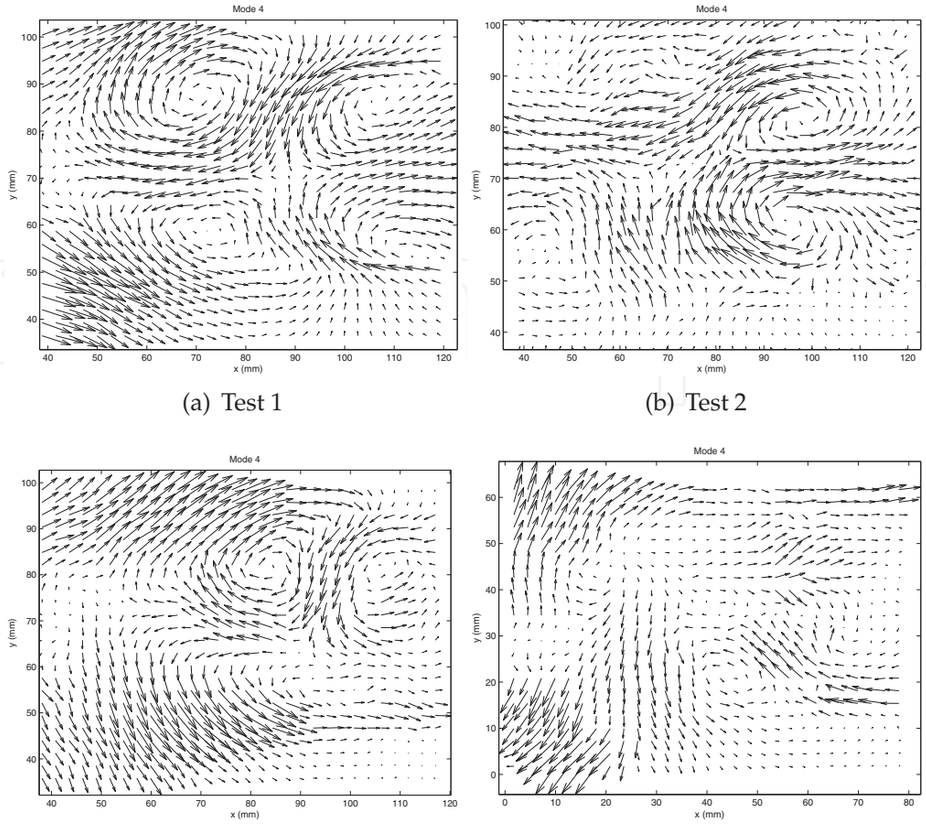

(a) Test 1 (b) Test 2

(c) Test 3 (d) Test 4

Fig. 17. Vector plots of the fourth mode shape for the four different tests

relative importance changes between tests. This phenomenon may provide justification for the assertion presented here concerning the higher modes, i.e. that modes higher than 3 represent transitional effects.

5. Conclusions

The feasibility of applying Proper Orthogonal Decomposition to experimentally measured flows around vibrating structures has been demonstrated. It has been shown that this type of decomposition analysis can provide some very interesting data about the observed flows, such as the dominant mode shapes and frequencies. Furthermore, it was shown that structural vibrations can be detected by the POD procedure applied on PIV flow visualization data using an output-only approach.

By considering the cylinder structural response as a forcing function, it is possible to create input-output POD models, whereby the generalized coordinates can be obtained from Frequency Response Functions relating the cylinder displacement response to the generalized coordinates themselves. It is shown that such FRFs feature two main frequency components, the mean flow frequency (i.e. 0Hz) and the vortex shedding frequency. Therefore, they are independent of the structural response frequency.

6. References

Cipolla, K. M., Liakopoulos, A. & Rockwell, D. (1998). Quantitative imaging in proper orthogonal decomposition of flow past a delta wing, *AIAA Journal* 36(7): 1247–1255.

Dowell, E. H., Hall, K. C. & Romanowski, M. C. (1998). Eigenmode analysis in unsteady aerodynamics: Reduced order models, *Applied Mechanics Reviews* 50(6): 371–385.

Hall, K. C. (1994). Eigenanalysis of unsteady flows about airfoils, cascades, and wings, *AIAA Journal* 32(12): 2426–2432.

Kim, Y., Rockwell, D. & Liakopoulos, A. (2005). Vortex buffeting of aircraft tail: Interpretation via proper orthogonal decomposition, *AIAA Journal* 43(3): 550–559.

Lie, T. & Farhat, C. (2007). Adaptation of aeroelastic reduced-order models and application to an F-16 configuration, *AIAA Journal* 45(6): 1244–1257.

Lumley, J. L. (1967). Atmospheric turbulence and radio wave propagation, Nauka, Moscow, pp. 116–178.

Tang, D., Kholodar, D., Juang, J. & Dowell, E. H. (2001). System identification and proper orthogonal decomposition method applied to unsteady aerodynamics, *AIAA Journal* 39(8): 1569–1576.

Tutkun, M., Johansson, P. B. V. & George, W. K. (2008). Three-component vectorial proper orthogonal decomposition of axisymmetric wake behind a disk, *AIAA Journal* 46(5): 1118–1134.

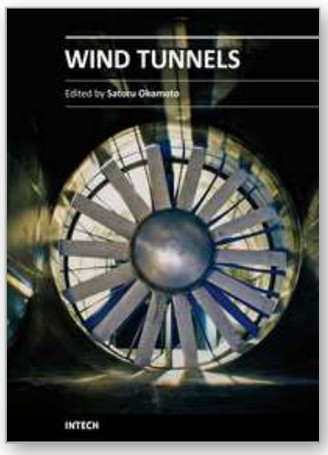

Wind Tunnels

Edited by Prof. Satoru Okamoto

ISBN 978-953-307-295-1

Hard cover, 136 pages

Publisher InTech

Published online 10, February, 2011

Published in print edition February, 2011

Although great advances in computational methods have been made in recent years, wind tunnel tests remain essential for obtaining the full range of data required to guide detailed design decisions for various practical engineering problems. This book collects original and innovative research studies on recent applications in wind tunnel tests, exhibiting various investigation directions and providing a birdâ€™s eye view on this broad subject area. It is composed of seven chapters that have been grouped in two major parts. The first part of the book (chapters 1â€“4) deals with wind tunnel technologies and devices. The second part (chapters 5â€“7) deals with the latest applications of wind tunnel testing. The text is addressed not only to researchers but also to professional engineers, engineering lecturers, and students seeking to gain better understanding of the current status of wind tunnels.ã€€Through its seven chapters, the reader will have an access to a wide range of works related to wind tunnel testing.

How to reference

In order to correctly reference this scholarly work, feel free to copy and paste the following:

Thomas Andrianne, Norizham Abdul Razak and Grigorios Dimitriadis (2011). Flow Visualization and Proper Orthogonal Decomposition of Aeroelastic Phenomena, Wind Tunnels, Prof. Satoru Okamoto (Ed.), ISBN: 978-953-307-295-1, InTech, Available from: http://www.intechopen.com/books/wind-tunnels/flow-visualization-and-proper-orthogonal-decomposition-of-aeroelastic-phenomena

INTECH
open science | open minds

InTech Europe
University Campus STeP Ri
Slavka Krautzeka 83/A
51000 Rijeka, Croatia
Phone: +385 (51) 770 447
Fax: +385 (51) 686 166
www.intechopen.com

InTech China
Unit 405, Office Block, Hotel Equatorial Shanghai
No.65, Yan An Road (West), Shanghai, 200040, China
中国上海市延安西路65号上海国际贵都大饭店办公楼405单元
Phone: +86-21-62489820
Fax: +86-21-62489821

IntechOpen